Growing oxide thin films in a low-energy electron microscope

Torren, A.J.H. van der

5

Imaging pulsed laser deposition growth of homo-epitaxial $SrTiO_3$ by Low-Energy Electron Microscopy

By combining low-energy electron microscopy with in-situ pulsed laser deposition we have developed a new technique for film growth analysis, making use of both diffraction and real-space information. Working at the growth temperature, we can use: the intensity and profile variations of the specular beam to follow the coverage in a layer-by-layer fashion; real-space microscopy to follow e.g. atomic steps at the surface; and electron reflectivity to probe the unoccupied band structure of the grown material. Here, we demonstrate our methodology for homo-epitaxial growth of $SrTiO_3$. Interestingly, the same combination of techniques will also be applicable to hetero-epitaxial oxide growth, largely extending the scope of research possibilities.

This chapter has been accepted as:

A.J.H. van der Torren, S.J. van der Molen, J. Aarts,
Imaging pulsed laser deposition growth of homo-epitaxial $SrTiO_3$ by Low-Energy Electron Microscopy
to be published in Nanotechnology

5.1 Introduction

Heterostructures of complex oxides have attracted great interest due to the possibility of combining a variety of physical properties by stacking multiple materials. Especially the 2-dimensional electron gas formed between the band insulators $SrTiO_3$ and $LaAlO_3$ has proven a fascinating research theme.[1,2]. The electronic properties of this electron gas are highly dependent on the substrate surface and the growth conditions[3–5].

To gain better control over the material properties, in-situ monitoring the growth, is of great importance. For the growth of these complex oxides, pulsed laser deposition (PLD) is the most widely used method to obtain high film quality. In-situ reflection high energy electron diffraction (RHEED) is commonly used for the growth monitoring, enabling layer-by-layer growth control[6–8]. However, this method only gives integral information and lacks spatial resolution. Spatially resolved measurements have been performed by scanning tunneling microscopy (STM)[9,10] and atomic force microscopy (AFM)[11], but these techniques can only be used after growth and not for in-situ monitoring. By combining PLD with low-energy electron microscopy (LEEM), we introduce a new possibility for layer-by-layer growth control combined with spatial resolution.

Here we present our development of pulsed laser deposition in a LEEM. We demonstrate this technique and the various imaging techniques that become available to study growth, in this case the growth of homo-epitaxial $SrTiO_3$. We show layer-by-layer growth control by spot-profile-analysis low-energy electron diffraction (SPA-LEED), while real-space images offer information on the terrace steps and surface morphology. Also, using energy-dependent electron reflectivity, we observe that the used growth conditions change the electronic structure.

5.2 Experimental

5.2.1 LEEM

The experiments were performed in the "Escher" LEEM setup, an aberration corrected LEEM facility at Leiden University[12–15]. In principle, LEEM is a form of microscopy that makes use of low-energy electrons to create highly surface sensitive images. However, by now, LEEM has become an umbrella term for a diverse set of techniques that can all be applied in-situ and in real time. For a LEEM to perform optimally, high energy electrons are required for the electron optics to work best, while the energy at the sample has to be close to zero. In order to achieve this, electron gun and sample are lifted to -15 kV and -15 kV + E_0 respectively, with the rest of the machine grounded, to accelerate and decelerate the electrons. This results in a high electric field between the objective lens and the sample which are only 1.5 mm apart. By changing this field slightly, the landing energy E_0 of the electrons at the sample can be tuned between zero and a few hundred electron volts. After interaction with the sample, the same field accelerates the electrons back towards the objective lens after which they are deflected towards the aberration corrector and finally to the projector column. An essential part is the magnetic

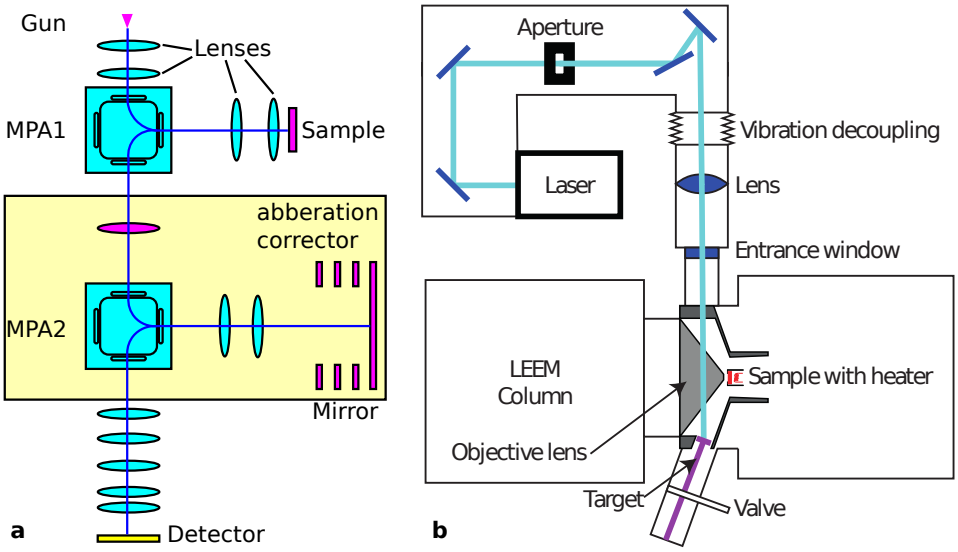

FIGURE 5.1: a) Sketch of the LEEM imaging system. Blue line shows the path of the electrons. The magnetic prism arrays are indicated by MPA1 and MPA2. b) The pulsed laser deposition setup incorporated into the LEEM. The target, objective lens and sample are to scale, the other components are not. The full laser path is enclosed for safety reasons.

prism array (MPA) splitting the pathways of the incoming electrons from the gun and outgoing electrons towards the detector. Images are finally obtained by amplifying the signal with a multichannel plate and converting the electrons to photons with a phosphor screen. The signal is then detected by a 12-bit ccd camera. A detailed sketch of the full imaging system is shown in figure 5.1(a).

5.2.2 In-situ pulsed laser deposition

The in-situ PLD system was designed along the following lines: The target-to-sample position was chosen to be between 40 and 60 mm as used in many PLD setups. For optimal performance of the microscope, the positions of sample and objective lens are fixed. This combination resulted in the target position as shown in figure 5.1(b). The target is placed on a linear transfer arm, allowing to change the target-to-sample distance. Every sample grown is ablated from a different area by rotating the target. A valve is added to allow replacement of the target without breaking the vacuum of the sample chamber. For the pulsed laser deposition a KrF excimer laser (Coherent COMPex Pro 201), 248 nm wavelength, is used. A uniform part of the laser spot is selected by a 5 x 15 mm aperture which is imaged on the target using a lens with a 407 mm focal length. This results in a 1/7 times magnification at the target. The laser hits the target under an angle of 22 degrees along the long side and 36.5 degrees along the short side of the laser beam, resulting in a 0.9 x 2.3 = 2.1 mm^2 exposed area on the target. For the fluence calculation,

the energy is measured right after the aperture and a loss at the entrance window of 8% is taken into account. In order to change the fluence the power of the laser or the magnification of the imaging system can be changed. The sample-to-target position for the samples discussed in this paper was chosen to be 50 mm.

The material plume created after ablation from the target contains charged particles. These particles would break down the high electric field between objective lens and sample, with the risk of damaging the sample. In order to combine the low-energy electrons with the PLD we perform the deposition and imaging alternating in time. Before deposition, the ppm-stable voltage supply is ramped down in less than 15 seconds. The laser is started once the voltage is below 2 kV and will apply the first deposition pulses when the field is only several tens of volts. When the deposition is finished the sample voltage is automatically ramped up and is stable again with ppm stability at 15 kV within 11 seconds. The sample can now be imaged. We take diffraction images over an energy range typically from 0 to 30 eV, from which we can obtain film properties and film thickness as will be discussed in the results section. More imaging techniques can be added if required. By repeating this cycle of deposition and imaging many times per atomic layer, the growth can be studied carefully. In practice, a balance needs to be found between the need for information and the growth time for a layer. Although the typical growth time is 30 s per monolayer, it takes about 25 minutes for the deposition of one unit cell when basic characterization is performed for every 0.1 unit cell. During the whole experiment, the sample is heated with an electron bombardment heater from the back. Stable deposition and imaging can be done up to 1000 °C and 10^{-4} mbar of oxygen. The background pressure of the system is 10^{-9} mbar and by differential pumping these UHV conditions are preserved in the the electron gun and projector column.

5.2.3 LEEM extensions

To be able to obtain maximum information from the diffraction images, spot profile analysis of the low-energy electron diffraction spots (SPA-LEED) is performed. However, in the typical range of measured energies the variation in intensity of the reflected electrons can be up to almost 10^4. This makes small signals undetectable with the 12-bit CCD camera (image depth: 4096). Dynamically changing the signal amplification solves this problem and is achieved by automatically adapting the channel plate gain. In this way, the maximum intensity on the CCD can be kept around 75% of its maximum, resulting in maximal image depth to resolve the spot profiles without damaging the channel plates. We characterized our channel plates and found the gain to follow $I = (I_{cmr} - b)e^{-GV_{cp}}$, where I_{cmr} is the intensity measured by the camera, b the background signal, mainly caused by the CCD readout noise, V_{cp} is the voltage over the channel plates in kV, G is the gain and I is the final intensity. The gain was calibrated to be equal to 20 kV^{-1}. Realistic values of the channel plate voltage lie between 0.9 kV and 1.7 kV allowing for more than six orders of magnitude range in intensity. During the measurement of an IV-curve (the intensity versus incoming-electon-energy), we calculate the channel

plate voltage required to saturate the CCD up to 75% after every image. This calculated channel plate voltage is used to capture the next image. By taking small steps through energy we expect the next image to be close in intensity to the current image, thus falling within range of the camera without further adjustments. By placing an aperture around the appropriate diffraction spot we avoid burning the channel plates due to other bright spots. Using this method we also optimized our earlier developed technique of angle-resolved reflection electron spectroscopy (ARRES)[16]. This technique will be further explained in section 5.3.4.

5.2.4 Sample preparation

Single crystals from Crystec GmbH were used as PLD target and as substrates for growth. The target-crystals were used as-received without further treatment while the sample substrates were prepared to be TiO_2-terminated. To obtain the TiO_2-termination, substrates were ultrasonicated in demineralized-water, etched for 30 s in buffered HF and annealed for one hour under oxygen flow[17]. The surface termination is verified by atomic force microscopy (AFM). Three samples were measured and will be called A to C. For real space experiments on sample B, markers were created to correct for sample drift. These markers are made by e-beam lithography and Ar-ion etching, and provide clear contrast in LEEM. For the PLD growth a pressure of 5×10^{-5} mbar was used for all samples and a 1 Hz repetition rate. Laser fluencies and growth temperatures for the three samples were as follows: sample A (1.4 J/cm^2, 665 °C), sample B (1.4 J/cm^2, 800 °C) and sample C (1 J/cm^2, 690 °C). Temperatures were measured by a pyrometer set to an emissivity of 0.8.

5.3 Results and discussion

The homo-epitaxial growth of $SrTiO_3$ strongly depends on the growth conditions. In the following we will show how the wide range of imaging techniques available in the LEEM allows in-situ characterizations of this growth.

Figure 5.2(a) shows a diffraction pattern of the bare $SrTiO_3$. A square surface net is clearly visible as well as traces of a 2x1 reconstruction. This surface reconstruction is described in earlier research[19–23]. Our temperature and pressure are very comparable to those used by Hesselberth *et al.*[23], who reported the reconstruction to form in UHV between 600 °C and 800 °C and to disappear in an oxygen pressure of 2×10^{-4} mbar. The origin of the reconstruction is believed to be oxygen loss. Our oxygen pressure of 5×10^{-5} mbar is in an intermediate regime where probably only part of the oxygen disappears, resulting in only a small amount of reconstruction.

More information can be obtained from the diffraction pattern by studying the shape and intensity of the specular beam. Figure 5.2(b) shows its maximum intensity as a function of landing energy. These so-called IV-curves, which measure the reflectivity of the surface, are correlated to the unoccupied band structure of the sample as we will discuss in section 5.3.4. For now we use it as a fingerprint of the

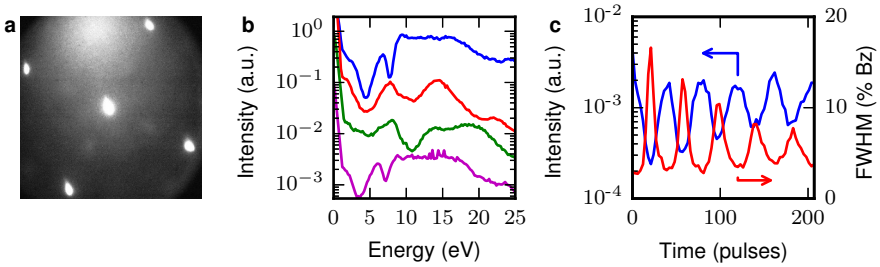

FIGURE 5.2: a) Diffraction pattern at bare TiO_2-terminated $SrTiO_3$ at 17 eV. A square surface net is visible, and traces of a 2x1 surface reconstruction. b) Maximum intensity versus landing energy of the specular spot for bare $SrTiO_3$ (blue, top) and after depositing 200 pulses of $SrTiO_3$ (red, 2nd from top). A reference curve on SrO-terminated $SrTiO_3$ substrate[18] (green, 3rd from top) and finally, an IV-curve after ex-situ annealing in an oxygen flow at 950 °C for one hour (magenta, bottom) are also shown. Data are taken on sample A. Curves are shifted for clarity. c) Maximum intensity (blue) and FWHM (red) of the specular spot versus layer thickness at a landing energy of 32 eV for sample A grown at 1.4 J/cm^2, 700 °C. The FWHM is presented in % Bz, the percentage of the Brillouin zone as measured by the average distance between the specular and first order spots.

material. Clear differences can be observed between bare TiO_2-terminated $SrTiO_3$ (figure 5.2(b), blue line, top) and the IV-curve taken after growth at sample A (figure 5.2(b), red line, 2nd from top). The IV-curve has strongly changed, in particular between 10 and 20 eV. This can both be due to the low oxygen pressure and/or be the result of off-stoichiometric (Sr/Ti ratio) growth. To investigate if off-stoichiometric growth could lead to Sr-excess on the surface, changing our IV-curve away from the TiO_2-termination fingerprint, we compare our results with a SrO-terminated $SrTiO_3$ sample. A sample with a double layer of SrO on TiO_2-terminated $SrTiO_3$ was grown in a different PLD system[18] and the resulting IV-curve is shown in figure 5.2(b) (green line, 3rd from top). This curve of SrO-termination is very similar to the after growth (red line, 2nd from top) curve for energies up to 15 eV, suggesting the presence of excess SrO. The excess SrO should be removable by the etching step performed to obtain TiO_2-terminated $SrTiO_3$. To confirm this, the IV-curve result after re-etching the grown surface in HF and annealing in oxygen flow for one hour at 950 °C is shown in figure 5.2(b) (magenta line, bottom). This IV-curve shows again the fingerprint of TiO_2-termination, confirming the grown $SrTiO_3$ had an excess of SrO on the surface.

5.3.1 Following the growth

Figure 5.2(c) show the maximum intensity (blue) and the full width at half maximum (FHWM) (red) versus growth time of the specular beam at a landing energy of 32 eV. The FWHM here is determined by averaging the horizontal en vertical sections of 60 pixels from the center of the specular beam and fitting the result

by a single Lorentzian function of which the FWHM can be easily obtained. Even in cases where the spot shows structure as will be encountered later on, the single Lorentzian fit results in a reasonable approximation of the FWHM. The FWHM is presented in units of %Bz, where 100 %Bz is the size of the Brillouin zone determined as the averaged distance between the specular and first order spots of the substrate, measured as 294 pixels on the camera.

Clear oscillations, fading out with thickness, can be observed. The FWHM is out of phase with the intensity as expected. The oscillations are correlated with the surface roughness. For flat surfaces i.e. multiples of a full unit cell grown, the diffraction pattern is sharp (i.e. small FWHM, high intensity). When material is deposited, the surface roughens and the diffraction spots broaden (i.e. large FHWM, low intensity).

From these oscillations we can conclude layer-by-layer growth for the first unit cells grown. The damping is a result of a change in growth mode to bigger islands, possibly caused by a change from layer-by-layer growth to a more three dimensional growth.

5.3.2 Real space

Growth can also be imaged in real space. Figure 5.3 shows LEEM bright field images for every half unit cell grown. For the full unit cells we observe a clear phase

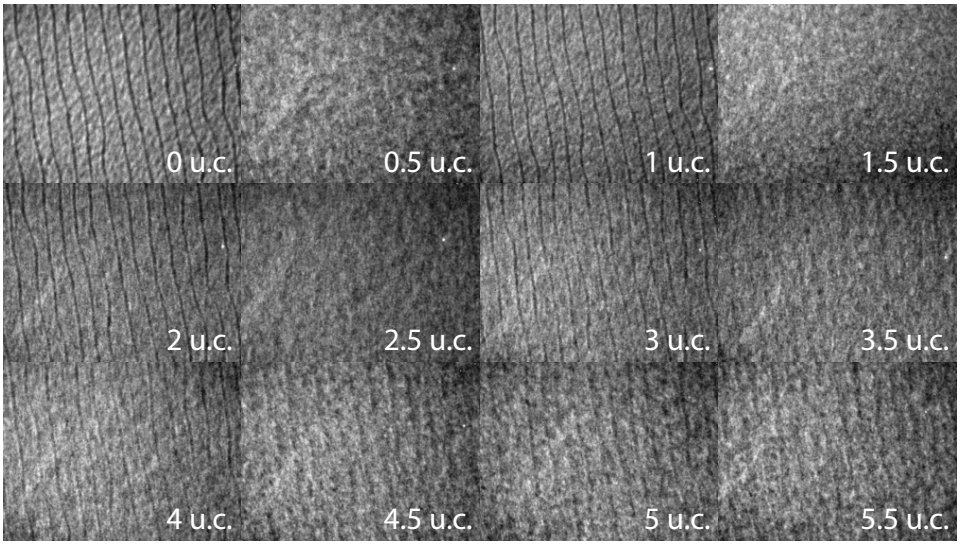

FIGURE 5.3: Normalized bright field images for every half unit cell up to 5.5 u.c, taken at 18 eV on sample B grown at a fluence of 1.4 J/cm^2. For full unit cell, terrace steps are visible as black lines by phase contrast. For half unit cell coverage the contrast disappears. At thicker layers 3D growth makes the intensity oscillations fade out.

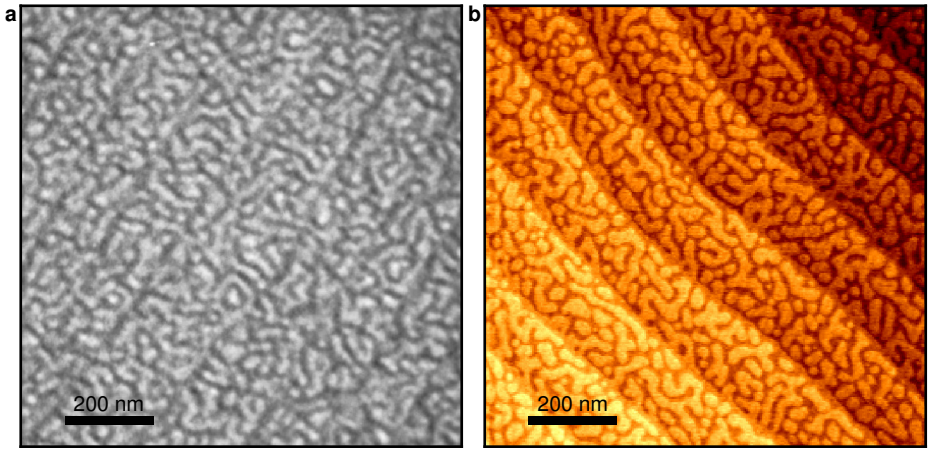

FIGURE 5.4: a) Bright field image at 13.6 eV after growth on sample C, grown at 700 °C and 1 J/cm^2. b) AFM image at same sample, but different area.

contrast at the terrace edges, visible as black lines due to destructive interference. On the other hand, at half unit cell coverage, the contrast has disappeared. The deposited material creates steps everywhere on the terrace, which are too small to detect. For thicker layers we also observe non-perfect growth. The step edges become blurred at full layer coverage, while for half layer coverage they do not fully disappear. Furthermore the real space images show that the step edges do not move, i.e. there is no step flow growth at this temperature.

In figure 5.4(a) we show a sample C which is grown with a fluence of 1 J/cm^2, instead of 1.4 J/cm^2. This changes the growth mode as can be clearly seen in the bright field image figure 5.4(a) and AFM image figure 5.4(b). The islands formed during the growth of a new layer are much bigger than in the other samples and can be clearly distinguished in bright field and AFM. These images are taken after growth of 225 pulses, just under 10 unit cells.

5.3.3 Spot-profile-analysis low-energy electron diffraction

Combining energy dependence (figure 5.2(b)) and growth time (figure 5.2(c)) for all energies one can create a full map. The specular beam intensity and FWHM variations can actually be measured at all energies, which results in the maps in figure 5.5(a), (b).

We observe a regular pattern in energy as well as in time. This is most clearly seen in the FWHM image of figure 5.5(b). To understand the energy dependence, we converted the energy axis to scattering phase[24] as shown on the axis on the right hand side of figure 5.5. The scattering phase is defined as $S = \frac{k_\perp d}{2\pi}$, with d the height of a unit cell $SrTiO_3$ and $k_\perp$ the out-of-plane wave vector. For the specular

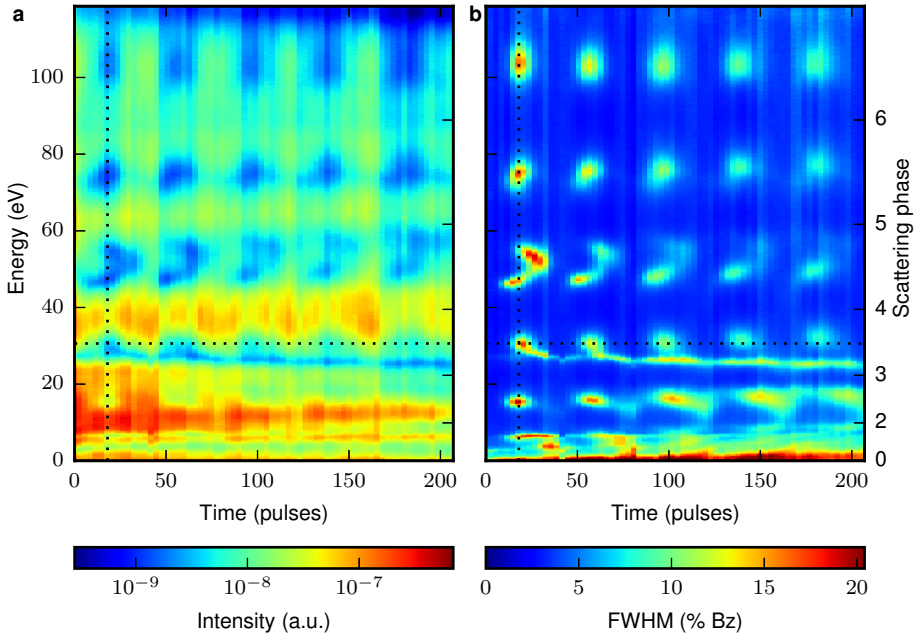

FIGURE 5.5: A map with intensity (left) and FWHM (right) of the specular beam on sample A. On the x-axis the time in units of pulses deposited is plotted while on the y-axis energy (left) or scattering phase (S) (right) is shown. S is defined in the text. The oscillations in energy follow the oscillations expected from the scattering phase. The peak splitting at S = 4.5 is not understood. Horizontal dotted line corresponds with the energy used for figure 5.2 and the vertical dotted line with half a unit cell where the data in figure 5.6 is taken.

spot $k_\perp = k$ (i.e. there is no in-plane component) and $S = \frac{kd}{2\pi} = 2d\sqrt{\frac{E(eV)}{150.4}}$. Here the zero of the energy, which depends on the gun potential and the work function of the sample, is determined by aligning the integer scattering phase values to the minima of the FWHM oscillations. When S is integer the electrons are in the in-phase (Bragg) condition. In this Bragg condition the electrons constructively interfere and are insensitive to the surface roughness. The diffraction spot is always sharp, i.e. the FWHM is low. For half integer values the electrons are in the out-of-phase (anti-Bragg) condition and destructively interfere at the terrace edges. When half a unit cell is grown the surface roughness is maximal (at least when the growth mode is island growth) and the specular beam has its maximum width. The effect of the scattering phase is more clear from the figure 5.6, where maximum intensity (blue) and FWHM (red) are plotted as function of scattering phase S for 1/2 unit cell of homo-epitaxial $SrTiO_3$. The scattering phase is in good agreement with the FWHM oscillations, except for S = 4.5 where the FWHM spot is split.

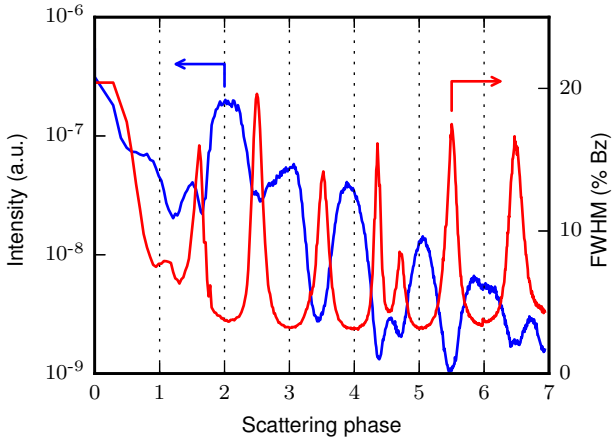

FIGURE 5.6: Maximum intensity (blue) and FWHM (red) of the specular beam versus scattering phase (S) after growth of 0.5 unit cell of homo-epitaxial $SrTiO_3$. The FWHM shows clear minima at integer values of the scattering phase and maxima at half integers. An exception is S = 4.5 where we observe a minimum instead of a maximum.

The cause of this splitting, which is also clearly visible in figure 5.5(b), is not understood. Other samples we measured showed the same behavior. We also note that for energies with a scattering phase below one, the interference signal deteriorates since not all electrons touch the surface any more before starting the return path.

Figure 5.7 presents a detailed view on the spot profiles at half a unit cell homo-epitaxial growth of $SrTiO_3$. The spot profiles in the anti-Bragg condition are broader than in the Bragg condition and they are actually split into two peaks, indicating a new diffraction condition caused by a regular terrace structure. This peak splitting is not found for S = 1.5 and S = 4.5. For S = 1.5 the electron wavelength of 0.55 nm is probably too large to resolve this terrace structure and at S = 4.5 we observe a small but sharp peak in agreement with the minimum observed in the FWHM in figure 5.6, which we cannot explain.

From the spot shape a more quantitative result can be extracted. The newly grown material forms small islands on the surface, slowly filling up a full layer. The characteristic parameters of this island formation are the average island size and the island size distribution width. These parameters can be extracted from the diffraction spot shape as discussed in ref. [25]. As an illustration the spot profiles for consecutive (n+$\frac{1}{2}$) unit cells (n integer) at S = 6.5 are plotted in figure 5.8(a), starting with 0.5 unit cell (blue, top) up to 4.5 unit cell (magenta, bottom).

These spot profiles can be reasonably well fitted with two Lorentzians, mirrored

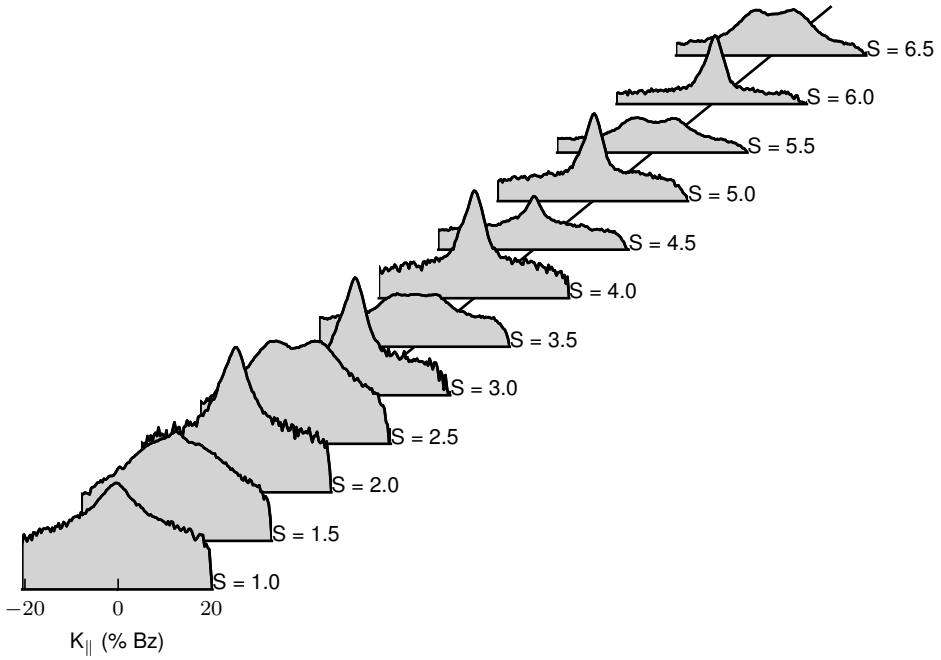

FIGURE 5.7: The beam shape vs scattering phase (S) for a half unit cell $SrTiO_3$ grown on sample A. The plot is on a log scale with background subtracted.

around the Brillouin zone center $x = 0$, as follows:

$$L_{double}(x) = A\left(\frac{\Gamma^2}{\Gamma^2 + (x - x_0)^2} + \frac{\Gamma^2}{\Gamma^2 + (x + x_0)^2}\right)$$

where A is the amplitude, 2Γ the FWHM of the Lorentzian and $2x_0$ the separation of the Lorentzians. Fits are shown in figure 5.8(a) as dotted lines. For very sharp island size distributions the diffraction spot would be split in two separate Lorentzians and the island size s_{island} can be obtained from the peak splitting $2x_0$. In our case the Lorentzians are strongly broadened and the peak splitting $2x_0$ and FWHM 2Γ are strongly correlated. Wollschläger[25] modeled the spot shape for the transition from sharp to broad island size distributions and the effect on the FWHM and spot splitting when this spot shape is approximated by two Lorentzians. In figure (3b) of his paper he plots the result for broad distributions, i.e. where the ratio of the standard deviation (σ) and island size (s_{island}) is greater than $\frac{\sigma}{s_{island}} > 0.6$. Figure 5.8(b) shows the island size s_{island} (blue, top) and distribution width σ (red, bottom) as obtained by applying the results of figure (3b) from Wollschläger on Γ and x_0. The ratio of σ/s_{island} confirms we are in the broad distribution limit.

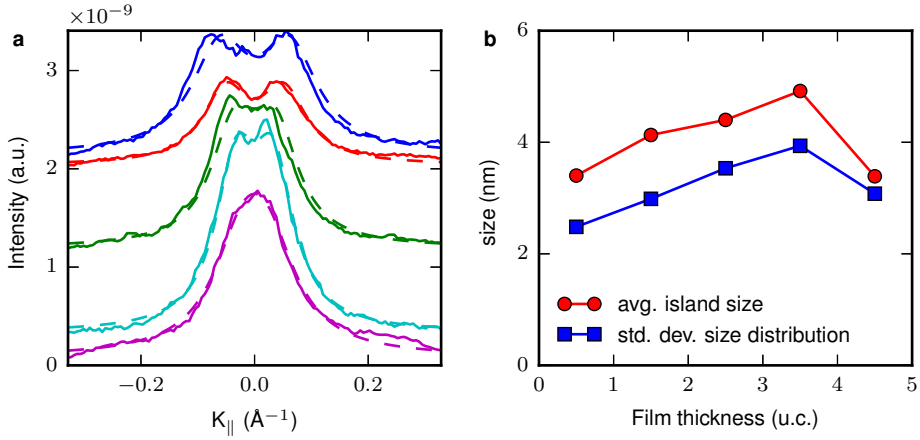

FIGURE 5.8: a) The beam profile at S = 6.5 on sample A, depending on layer thickness, shifted for clarity. From top to bottom 0.5, 1.5, 2.5, 3.5, 4.5 u.c. The spots become sharper over time, except at 4.5 u.c., indicating bigger island sizes. b) The average island size s_{island} versus layer thickness (blue, top) and the standard deviation of island size distribution σ (red, bottom).

Compared to literature our terraces sizes are relatively small. It is close to findings of Phark *et al.*[10], while Xu *et al.*[11] found much bigger island sizes, in the order of tens of nanometers. This can probably be explained by the relative low temperature of 670 °C, which is closer to Phark *et al.* (580 °C) and lower than the one used by Xu *et al.* (800 °C). The advantage of our technique above the earlier used AFM and STM is the continuous tracking over thickness at growth conditions, without the need for cooling down or sample transfer.

5.3.4 Angle-resolved reflection electron spectroscopy

As stated earlier the IV-curve in figure 5.2(b) is correlated with the unoccupied band structure of the material. In particular, the electron reflection probability is high when there is a band gap at that specific energy while the reflection probability is low when an electron can couple into an electronic state[(1)]. Here zero energy corresponds with the vacuum level and thus the states probed are above the vacuum level, i.e. the unoccupied band structure. Figure 5.9(a) shows how the IV-curves change with time when homo-epitaxial $SrTiO_3$ is grown on sample A. For the $SrTiO_3$ substrate there is a small band gap at 8 eV and a large band gap between 10 and 17 eV. The small band gap stays constant during growth while the large band gap sharpens to only a small band gap around 15 eV. The change is more clear if we not only look at the landing energy E_0 but also at the in-plane momentum of the electron, $k_\parallel$. The electron reflectivity now depends on (E_0, $k_\parallel$) and a full

[(1)] Multiple scattering effects can influence the result.

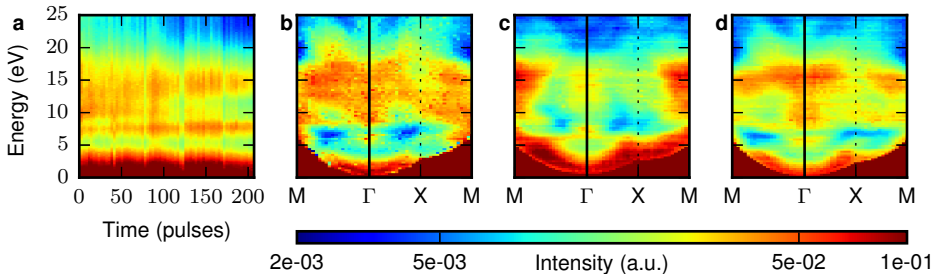

FIGURE 5.9: a) IV-curves versus growth time for sample A grown at 1.4 J/cm^2. b) ARRES map on bare typical TiO_2-terminated $SrTiO_3$ (not on sample A). c) ARRES map on sample A after growth and d) ARRES map after reviving the surface by a single termination step.

unoccupied band structure map can be made. Mapping the full energy versus $k_{\|}$ behavior is called angle-resolved reflection-electron spectroscopy (ARRES) [16]. Changing the in-plane momentum is achieved by deflecting the electron beam just behind the electron gun. The resulting in-plane momentum can be determined from the position of the specular spot in the Ewald-sphere. In practice, the deflection of the beam allows to reach the Brillouin zone edge comfortably. Figure 5.9(b), (c) and (d) show ARRES maps for bare TiO_2-terminated $SrTiO_3$, for sample A after growth of 5 unit cells of $SrTiO_3$ and after a single termination procedure where the sample after growth is etched in a buffered HF and ex-situ annealed in an oxygen flow at 950 °C. The IV-curves shown earlier are vertical cuts at the Γ-point, as indicated with a vertical black line. The large band gap between 8 and 17 eV at the $SrTiO_3$ substrate extends to the direction of the M and X-point. This band gap strongly changes after the growth. It shrinks and is not connected towards the M and X-point anymore. The bands around 6 eV halfway towards the M and X-point have moved upwards, making space for a large band gap at the lowest energies. After the single termination procedure the band gap between 8 and 17 eV has recovered to a great extent and the band gap at the lowest energies has shrunk back to the size seen at the $SrTiO_3$ substrate. This is also clear in figure 5.2(b), where in particular the behavior around 6-8 eV changes. Here, the bare $SrTiO_3$ shows a dip, the sample after growth a peak, and the annealed sample again a dip. The single termination procedure appears to do two things. In the first place excess SrO which is collected on the surface due to the off-stoichiometric growth is removed. Secondly, the anneal step replenishes any oxygen vacancies that are created during growth. The two steps together regenerate the surface of the stoichiometric $SrTiO_3$.

5.4 Conclusion

In summary, combining LEEM with PLD provides a unique possibility to in-situ analyze the growth of perovskites by the possibility to combine SPA-LEED with

real space and unoccupied band structure information. We demonstrated this with the growth of homo-epitaxial $SrTiO_3$.

From the specular spot shape images and real space images we can conclude that the growth mode slowly changes from layer-by-layer growth to more 3 dimensional growth. Roughness oscillations slowly damp out, the size of the islands from which the newly grown layer forms slowly increases and in real space the difference between half and full unit cell grown disappears. The growth mode depends on the growth conditions. For low fluence we have seen microscopic island sizes, clearly distinguishable in real space. The electronic structure changes during the growth of homo-epitaxial $SrTiO_3$. This can be caused by off-stoichiometric growth as well as by oxygen vacancies due to the low oxygen pressure during growth. The excess SrO can be removed by buffered HF and the oxygen can be replenished by ex-situ annealing in an oxygen flow. These steps partially recover the ARRES map found in the stoichiometric $SrTiO_3$ substrate.

The full range of possibilities offered by LEEM clearly allows to perform thorough studies during growth of perovskites, making it possible to draw conclusions during growth without performing ex-situ studies afterwards.

References

[1] A. Ohtomo and H. Y. Hwang, *A high-mobility electron gas at the $LaAlO_3/SrTiO_3$ heterointerface*, Nature **427**, 423 (2004).

[2] S. Thiel, G. Hammerl, A. Schmehl, C. W. Schneider, and J. Mannhart, *Tunable Quasi-Two-Dimensional Electron Gases in Oxide Heterostructures*, Science **313**, 1942 (2006).

[3] M. P. Warusawithana, C. Richter, J. A. Mundy, P. Roy, J. Ludwig, S. Paetel, T. Heeg, A. A. Pawlicki, L. F. Kourkoutis, M. Zheng, M. Lee, B. Mulcahy, W. Zander, Y. Zhu, J. Schubert, J. N. Eckstein, D. A. Muller, C. S. Hellberg, J. Mannhart, and D. G. Schlom, *$LaAlO_3$ stoichiometry is key to electron liquid formation at $LaAlO_3/SrTiO_3$ interfaces*, Nature Communications **4** (2013).

[4] D. G. Schlom and J. Mannhart, *Oxide electronics: Interface takes charge over Si*, Nature Materials **10**, 168 (2011).

[5] A. Sambri, D. V. Cristensen, F. Trier, Y. Z. Chen, S. Amoruso, N. Pryds, R. Bruzzese, and X. Wang, *Plasma plume effects on the conductivity of amorphous-$LaAlO_3/SrTiO_3$ interfaces grown by pulsed laser deposition in O2 and Ar*, Applied Physics Letters **100**, 231605 (2012).

[6] G. Rijnders, Ph.D. thesis (2001).

[7] G. Koster, G. J. H. M. Rijnders, D. H. A. Blank, and H. Rogalla, *In situ initial growth studies of $SrTiO_3$ on $SrTiO_3$ by time resolved high pressure RHEED*, Materials Research Society symposia proceedings pp. 33–37 (1998).

[8] M. Lippmaa, N. Nakagawa, M. Kawasaki, S. Ohashi, Y. Inaguma, M. Itoh, and H. Koinuma, *Step-flow growth of $SrTiO_3$ thin films with a dielectric constant exceeding 104*, Applied Physics Letters **74**, 3543 (1999).

[9] S.-h. Phark, Y. J. Chang, and T. Won Noh, *Selective growth of perovskite oxides on $SrTiO_3$ (001) by control of surface reconstructions*, Applied Physics Letters **98**, 161908 (2011).

[10] S.-h. Phark and Y. J. Chang, *Nucleation and growth of primary nanostructures in $SrTiO_3$ homoepitaxy*, Nanoscale Research Letters **10**, 80 (2015).

[11] C. Xu, M. Moors, and R. Dittmann, *Impact of cation stoichiometry on the early stage of growth of $SrTiO_3$ deposited by pulsed laser deposition*, Applied Surface Science **359**, 68 (2015).

[12] R. Tromp, J. Hannon, A. Ellis, W. Wan, A. Berghaus, and O. Schaff, *A new aberration-corrected, energy-filtered LEEM/PEEM instrument. I. Principles and design*, Ultramicroscopy **110**, 852 (2010).

[13] S. M. Schramm, J. Kautz, A. Berghaus, O. Schaff, R. M. Tromp, and S. J. van der Molen, *Low-energy electron microscopy and spectroscopy with ESCHER: Status and prospects*, IBM Journal of Research and Development **55**, 1:1 (2011).

[14] S. M. Schramm, A. B. Pang, M. S. Altman, and R. M. Tromp, *A Contrast Transfer Function approach for image calculations in standard and aberration-corrected LEEM and PEEM*, Ultramicroscopy **115**, 88 (2012).

[15] R. Tromp, J. Hannon, W. Wan, A. Berghaus, and O. Schaff, *A new aberration-corrected, energy-filtered LEEM/PEEM instrument II. Operation and results*, Ultramicroscopy (2013).

[16] J. Jobst, J. Kautz, D. Geelen, R. M. Tromp, and S. J. van der Molen, *Nanoscale measurements of unoccupied band dispersion in few-layer graphene*, Nature Communications **6**, 8926 (2015).

[17] M. Kawasaki, K. Takahashi, T. Maeda, R. Tsuchiya, M. Shinohara, O. Ishiyama, T. Yonezawa, M. Yoshimoto, and H. Koinuma, *Atomic Control of the $SrTiO_3$ Crystal Surface*, Science **266**, 1540 (1994).

[18] C. Xu and R. Dittmann, *growth of SrO-terminated $SrTiO_3$ sample.*

[19] N. Erdman, K. R. Poeppelmeier, M. Asta, O. Warschkow, D. E. Ellis, and L. D. Marks, *The structure and chemistry of the TiO_2-rich surface of $SrTiO_3$ (001)*, Nature **419**, 55 (2002).

[20] N. Erdman and L. D. Marks, *$SrTiO_3$(001) surface structures under oxidizing conditions*, Surface Science **526**, 107 (2003).

[21] T. Kubo and H. Nozoye, *Surface structure of $SrTiO_3$(100)*, Surface Science **542**, 177 (2003).

[22] M. R. Castell, *Scanning tunneling microscopy of reconstructions on the $SrTiO_3$(001) surface*, Surface Science **505**, 1 (2002).

[23] M. B. S. Hesselberth, S. J. v. d. Molen, and J. Aarts, *The surface structure of $SrTiO_3$ at high temperatures under influence of oxygen*, Applied Physics Letters **104**, 051609 (2014).

[24] M. Horn-von Hoegen, *Growth of semiconductor layers studied by spot profile analysing low energy electron diffraction Part I1*, Zeitschrift fr Kristallographie - Crystalline Materials **214**, 591 (1999).

[25] J. Wollschlger, *Simple analysis of spot splitting due to diffraction at surfaces with atomic steps*, Surface Science **383**, 103 (1997).